Chapter 11

Radio and X-ray Emission from the Galactic Black Hole

Heino Falcke
Max-Planck-Institut für Radioastronomie, Bonn, Germany

To appear in: The Galactic Black Hole, Lectures on General Relativity and Astrophysics, H. Falcke and F.W. Hehl (eds.), IOP Publishing, Bristol (2002)

Summary: In this chapter the radio properties of the Galactic Center black hole (Sgr A*) are reviewed: variability, size and position from VLBI (Very Long Baseline Interferometry), spectrum, and polarization. Radio and X-ray emission are discussed within the framework of black hole plasma jet models and simple equations for the emission are derived. It is also shown that the radio emission can be used to actually image the event horizon of the black hole in the near future.

Contents

11.1 Introduction

We have already seen in Chapter **??** that the evidence for the presence of a dark mass in the Galactic Center is very strong. A central point mass of about $3 \cdot 10^6 M_\odot$ seems to coincide with the compact radio source Sgr A*. The existence of Sgr A* has always been considered a good sign for a black hole itself. In fact, based on analogous detections of compact radio cores in the nuclei of active galaxies, the existence of Sgr A* was predicted by Lynden-Bell & Rees (1971). Balick & Brown (1974) detected the source in one of the early VLBI (Very Long Baseline Interferometry) experiments and a couple of years later named it Sgr A* (by simply adding an asterisk to the name of the nuclear radio region Sgr A — see Palmer & Goss 1996 for an account of the history of naming sources in the Galactic Center).

Ever since, Sgr A* has been the focus of great attention. From the near-infrared speckle observations (Eckart, this volume) we know that it is at the very center of the gravitational potential. However, until today one is still unsure about the exact nature of the detected emission in radio and X-ray bands. On the other hand, understanding the radiation spectrum of Sgr A* will have important implications for all other supermassive black holes, since most galaxies will have black holes that are as inactive as the Galactic Center and we are investigating the low-power end on the black hole activity scale. In fact, surveys have shown that a large number of nearby galaxies host radio sources very similar to Sgr A* in our Milky Way (Wrobel & Heeschen 1984, Nagar et al. 2000, Falcke et al. 2000). Hence, what we learn about Sgr A* is quite typical for the (rather silent) majority of black holes in the universe.

In the following section we will attempt to summarize the main radio properties of the "Galactic Black Hole". In the subsequent sections we will try to explain the main emission characteristics of Sgr A* in an almost back-on-the-envelope fashion. Finally we will look ahead on how this source could finally make the theoretical concept of an event horizon observable in the near future.

11.2 Radio Properties of Sgr A*

Most of the direct information about Sgr A* is available at radio wavelengths. This includes the total intensity spectrum, the variability, the polarization, and the source structure. In the following we will go through these various issues step by step.

11.2.1 Variability of Sgr A*

First evidence for a a very compact structure in a radio source often comes from its variability. And indeed soon after its discovery, Sgr A* was es-

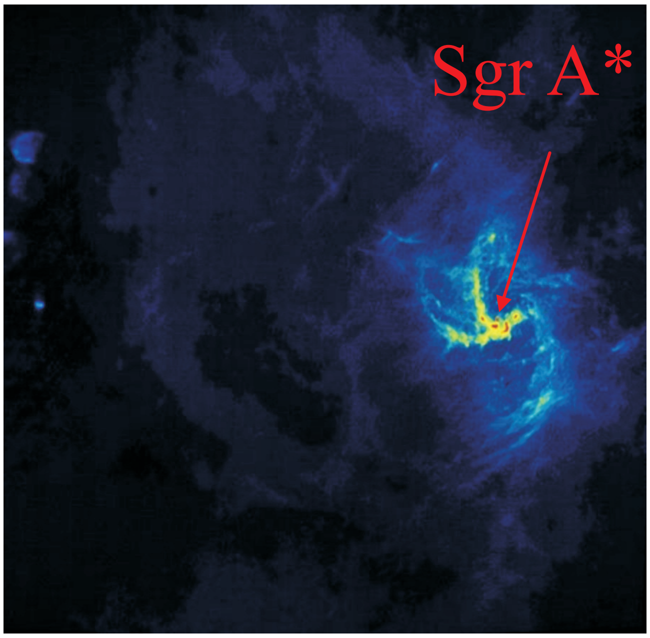

Figure 11.1 Sgr A West, a spiral-like pattern of thermal ionized gas that appears to be falling into the very center of the galaxy. Near its center is Sgr A*, a point-like radio source that many suspect is the nucleus of the Milky Way and indicates the presence of a black hole. Figure courtesy of Prof. K.Y. Lo

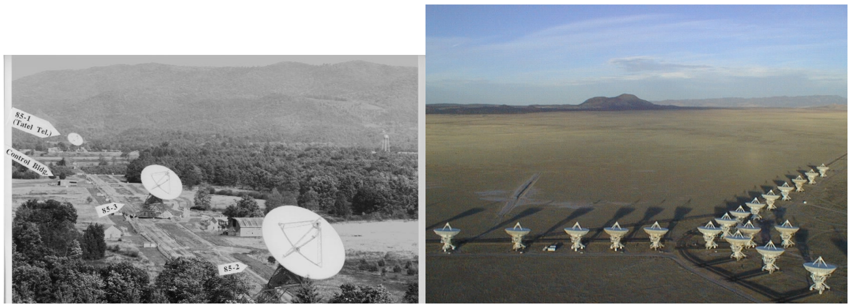

Figure 11.2 The Green Bank Interferometer (GBI; left) which was instrumental in detecting Sgr A* and the Very Large Array (VLA; right). Both interferometers are operated by the National Radio Astronomy Observatory (NRAO) in the United States and were extensively used to monitor the variability of Sgr A*.

tablished as a variable source (Brown & Lo 1982) and extended campaigns were set up to monitor this variability. The most extensive data sets were obtained using the Very Large Array (VLA) and the Green Bank Interferometer (GBI; see Fig. 11.2). The most recent data from these instruments are presented in Zhao, Bower, & Goss (2001) and Falcke (1999). The amplitude of variability can reach up to 200% for strong flares. The degree of variability seems to increase with increasing frequency. Strong flares seem to occur on time scales of 100 days (see Fig. 11.3). Zhao, Bower, & Goss (2001) even claim to have found a periodicity of 106 days on which such strong flares occur regularly. The shortest times scale of radio variability was probably found by Bower et al. (2002a) at 15 GHz: 20% within one hour.

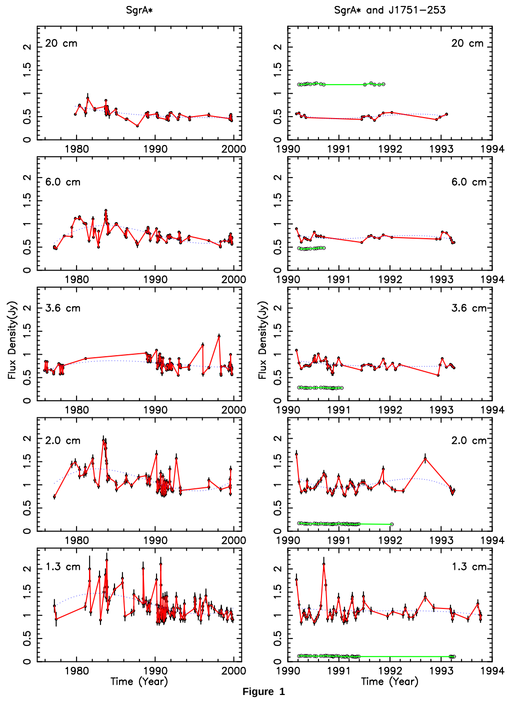

Figure 11.3 Variability of Sgr A* as observed with the VLA at different wavelengths (given in the top left corner of each frame). From Zhao, Bower, Goss (2001).

Some of the radio variability may be due to scintillation due to an foreground screen (see below), but at least the large-amplitude flares at higher radio frequencies are most likely of an intrinsic nature. The fastest variations are fundamentally limited by the source size. We can then convert the measured time scale τ and amplitude $\Delta S/S$ of the variability into a limit on the characteristic size R of Sgr A*. For a given maximum signal speed $v_{\rm max} \lesssim c$ in the emitting plasma, one obtains

$$R < (\Delta S/S)^{-1}\, \tau \cdot v_{\rm max}. \tag{11.1}$$

For $(\Delta S/S) = 20\%$ and $\tau = 1$ hr we get $R < 5 \cdot 10^{14}$ cm $\cdot(v_{\rm max}/c)$, which is 36 Astronomical Units (AU) or 4.5 milli-arcseconds (mas) at the Galactic Center distance of 8 kpc. Based on the variability time scale alone the radio emission therefore has to come from a region smaller than a planetary system. In fact,as we will learn in the next subsection, direct radio imaging shows that the emission comes from an even smaller scale.

Alternatively, taking the much longer 100 day time scale we find a characteristic size of $R < 2.7 \cdot 10^{17}$ cm $\cdot(v_{\rm max}/c)$ or 2.3 arcseconds. This is relatively large and does not appear to be a useful limit for the size of Sgr A*. It is more likely that this variability signals some other underlying physical process, e.g. a process related to the accreting material powering the source.

If the accreting gas is in orbit around the central point mass $M_\bullet$ the characteristic velocity will be set by the the Keplerian velocity[1] $v = \sqrt{GM_\bullet/R}$ and the corresponding time scale is set by $\tau = 2\pi R/v$, yielding

$$R \approx \left(\frac{\tau}{2\pi}\right)^{2/3} (GM_\bullet)^{1/3} = 0.9 \cdot 10^{15}\,\mathrm{cm}\, \left(\frac{\tau}{106\mathrm{days}}\right)^{2/3} \left(\frac{M_\bullet}{3 \cdot 10^6 M_\odot}\right)^{1/3}. \tag{11.2}$$

This corresponds to about 1000 Scharzschild radii or 8 mas. The accretion radius (Coker, this volume) of the hot X-ray gas in the Galactic Center is somewhat further out, but it is not impossible that instabilities in the capture process of surrounding gas by the black hole are the ultimate source of the slow, large-amplitude variability. If the flares are indeed periodic as claimed by Zhao, Bower, & Goss (2001), then one probably has to think of a star orbiting Sgr A* at this distance which modulates the accretion flow.

On the other hand, in stellar mass black holes, quasi-periodic signals are often related to beat and precession frequencies of accretion disks close to the black hole. If true, this can be used to derive informations about the black hole spin. Such a scenario has been considered by Liu & Melia (2002). Based on such a model and the 100 day periodicity, they derive a black hole spin parameter (e.g., Sec. 11.4) of Sgr A* of $a \simeq 0.1$. It is difficult to assess which of these interpretations is correct.

The fastest variations are expected at the shortest wavelengths, since high-frequency emission – in essentially all models for Sgr A* – is typically

[1] Note that the sound speed of infalling gas in optically thin accretion models is typically of similar order and hence the same numbers apply.

produced at the smallest scales. The problem with high-frequency measurements of Sgr A* is that these observations are extremely sensitive to weather and the low elevations of the source encountered in typical observations from the northern hemisphere. Because of the large confusing flux in the Galactic Center, interferometers have to be used. The flux density measured on an interferometer baseline can be artificially reduced by rapid changes in the atmospheric opacity and loss of coherence (of instrumental or atmospheric origin) which are difficult to track. Early observations (Wright & Backer 1993, Zylka et al. 1995) already indicated possibly strong variations in the sub-millimeter wavelength region. This was later strengthened by Tsuboi, Miyazaki, & Tsutsumi (1999) and very recently Zhao et al. (2001) claim relatively strong sub-millimeter flares in Sgr A* from measurements with the sub-millimeter array (SMA) in Hawaii. These results will certainly become more and more important in the years to come since, as we will see below, this emission most certainly comes directly from the immediate environment of the event horizon.

11.2.2 Size of Sgr A* – VLBI Observations

A major issue for a long time has been the exact size and structure of Sgr A*. In extragalactic sources the VLBI technique has allowed one to probe deep into the hearts of active galactic nuclei and resolved the radio structures into relativistically outflowing plasma jets (see, e.g., Zensus 1997). In a VLBI experiment radio telescopes distributed over a continent or the entire world are synchronized by atomic clocks and observe jointly one source. The incoming radio waves are digitized and stored (usually on magnetic tapes). Later, the digitized waves are correlated in a specialized computer recreating a virtual interferometer. Such a virtual interferometer will have a spatial resolution similar to that of a giant telescope with the diameter of roughly the separation of the individual telescopes (called "baselines"). This technique has yielded by far the highest resolution images in astronomy (i.e., 50 μarcseconds at 86 GHz). The image quality improves with the number of participating telescopes and the two major VLBI arrays today are the European VLBI Network (EVN) and the Very Long Baseline Array (VLBA) in the United States.

Of course, a prominent source such as Sgr A* has been a prime target for VLBI experiments over the last 25 years. It is from these observations that we have direct information on the size of the source – or at least have very tight upper limits.

It was, however, quickly realized that, despite its relative proximity, detecting the true structure of Sgr A* is unusually difficult compared to other galactic nuclei. The reason is that that interstellar material in the line line-of-sight towards the Galactic Center scatter broadens the VLBI image. This produces a characteristic λ^2-law (e.g. Scheuer 1968) for the size of Sgr

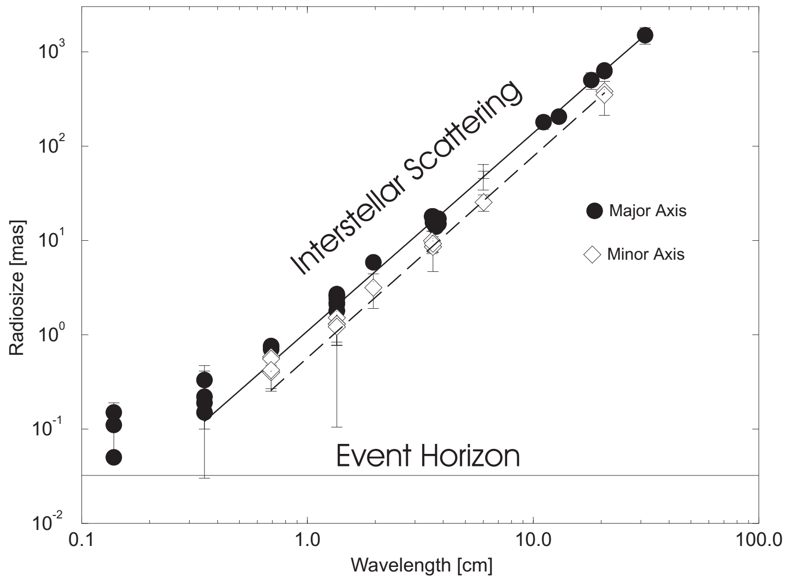

Figure 11.4 The major source axis (filled circles) of Sgr A* and the minor source axis (open diamonds) as measured by VLBI plotted versus wavelength (adapted from Krichbaum et al. 1999.). The inclined lines show the λ^2 scattering law and the horizontal line shows the size scale expected for the visual imprint of the event horizon (Falcke, Melia, Agol 2000).

A* (Davies, Walsh, & Booth 1976, van Langevelde et al. 1992, Yusef-Zadeh et al. 1994, Lo et al. 1998). The scattering size apparently has not changed over a decade (Marcaide et al. 1999). For that reason the *intrinsic* size and structure of Sgr A* remains obscure until today (Fig. 11.4 & 11.5). The measured size of Sgr A* is given by (Lo et al. 1998)

$$\theta_{\rm minor} = 0.76\,{\rm mas}\;(\lambda/{\rm cm})^2, \quad \theta_{\rm major} = 1.42\,{\rm mas}\;(\lambda/{\rm cm})^2. \tag{11.3}$$

The front line of this research is currently at wavelengths of 7mm and shorter. Lo et al. (1998) Krichbaum et al. (1993), and Krichbaum et al. (1998) claim to have seen evidence for a deviation from the scattering law at these wavelengths. Other experiments did not directly confirm this (Rogers et al. 1994, Bower & Backer 1998, Doeleman et al. 2001). The main problem is that Sgr A* is never above 25° elevation at the VLBA and mm-VLBI is strongly affected by the variable atmosphere. Significant distortions of the phase (of the radio waves) can happen on time scales of 10 seconds at the short wavelengths. Therefore mm-VLBI observations of

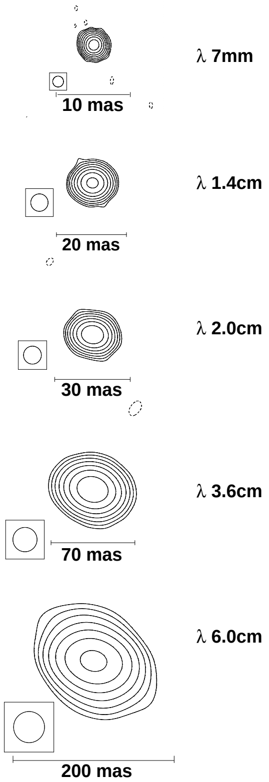

Figure 11.5 Contour plots of VLBA images of Sgr A* at wavelengths of $\lambda = 6.0, 3.6, 2.0, 1.35, \& \ 0.7$ cm. These images are smoothed to a circular beam of FWHM = 2.62 $\lambda_{cm}^{1.5}$ mas as shown on the left-bottom corner on each image. The contours are 2 mJy beam$^{-1}\times$ (-2, 2, 4, 8, 16, 32, 64, 128, 256). Figure from Lo et al. (1999).

Sgr A* are difficult to calibrate and are always subject of intense scrutiny and nagging doubts.

On the other hand, the rapid variability of Sgr A* with time scales of 10 minutes (X-rays) to 3 hours (15 GHz radio) suggests that time-variable structure may exist on similarly short time scales. We can estimate a scale for adiabatic cooling of a plasma by using Eq. 11.3, convert to a linear size at the Galactic Center distance $D_{\rm GC} = 8$ kpc, and divide by the maximal sound speed of a relativistic plasma (photon gas; see e.g. Königl 1980) $c_{\rm s} = c/\sqrt{3}$. We get

$$t_{\rm cool} \gtrsim \theta_{\rm major} D_{\rm GC}/c_{\rm s} = 1.3\,{\rm hrs}\left(\frac{\lambda}{7\,{\rm mm}}\right)^2. \tag{11.4}$$

Hence, if for example, matter is ejected during one of the big X-ray flares near the black hole it could in principle cool and fade away within a few hours at most radio wavelengths[2]. Consequently, there is no reason why VLBI observations separated by one day always have to look the same.

11.2.3 Position of Sgr A*

The exact location of Sgr A* is a very important factor for its interpretation. This allows one to investigate whether the source is indeed in the Galactic Center (and not behind) and to set a lower limit on its mass. The position can be determined relatively accurately with radio observations.

This requires the use of so-called "phase-referencing" observations. In this type of experiments the telescopes of a VLBI-array are switched rapidly from one source to another, where both sources should be within one isoplanatic patch of the atmosphere (typically 1° to 5°). Within this patch the radiation passes roughly through the same atmospheric irregularities. The switching also has to happen within the coherence time of the atmosphere—at mm-wavelengths the telescopes switch sources every 10 seconds. The phase-difference of the incoming wave fronts between the two observed sources can then be used to determine the relative positions of the sources. By fixing a grid of phase-referenced sources — radio quasars at cosmological distances – one can then establish an absolute coordinate system, called the International Celestial Reference System (ICRF; see Ma et al. 1998). Since 1997 the ICRF is the fundamental reference system of astronomy as adopted by the International Astronomical Union (IAU).

Attempts have been made to relate the *absolute* position of Sgr A* to bright background quasars. Averaging of VLA observations by Yusef-Zadeh, Choate, & Cotton (1999) yield a position for Sgr A* at the epoch 1992.4 of

$$\alpha(1950) = 17^h42^m29.3076^s \pm 0.0007s,\ \delta(1950) = -28°59'18.484" \pm 0.014" \tag{11.5}$$

$$\alpha(2000) = 17^h45^m40.0383s \pm 0.0007s,\ \delta(2000) = -29°00'2^8.069" \pm 0.014". \tag{11.6}$$

A position using VLBA observations was also derived by Rogers et al. (1994), which agrees with this position within 0.2". In yet another experiment Menten et al. (1997) were able to relate the position of Sgr A* to

[2] Note that Eq. 11.4 is based solely on the *observed* upper limit on the source size. Most models suggest that the intrinsic size of Sgr A* grows less rapidly than λ^2 (e.g. linearly) and hence the cooling time scale would grow accordingly slower.

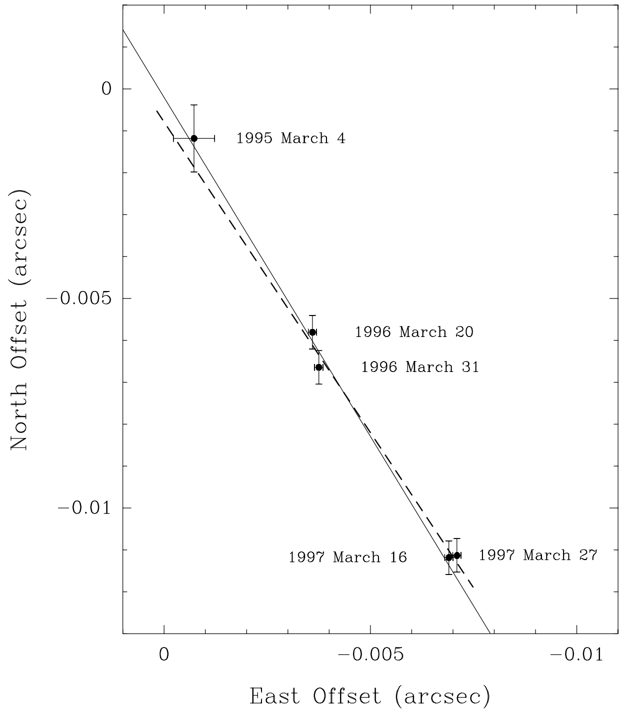

Figure 11.6 Position of Sgr A* relative to a background quasar (J1745–283) on the plane of the sky determined from VLBA observations. North is to the top and East to the left. Each measurement is indicated with the date of observation and $1-\sigma$ error bars. The dashed line is the best-fit proper motion, and the solid line gives the orientation of the Galactic plane. Figure from Reid et al. (1999).

the position of near-infrared stars (emitting a radio line) surrounding it. This allows one to locate Sgr A* in a near-infrared image and try to find a counterpart.

Finally, one can also measure the *relative* position of Sgr A* with respect to faint background quasars which are much closer than the ICRF reference sources. Assuming that these sources are without motion on the sky (because of their cosmological distances), Reid et al. (1999) (Fig. 11.6; see also Backer & Sramek 1999) find a proper motion for Sgr A* of -3.33 ± 0.1 mas yr^{-1} (E) and -4.94 ± 0.4 mas yr^{-1} (N), corresponding to -5.90 ± 0.35 mas yr^{-1} and $+0.20\pm 0.30$ mas yr^{-1} in Galactic longitude and latitude. This agrees very well with the apparent motion expected for a source at the Galactic center due to the *Galactic rotation of the solar system* (220 km s^{-1}). This implies that Sgr A* is indeed at the center of the Galaxy and has very little motion of its own ($v_{\mathrm{Sgr\,A*}} < 15\,\mathrm{kms}^{-1}$). This is interesting, since in Chapter **??** it was shown that stars near Sgr A* move in the deep potential well with velocities up to 1500 km s^{-1}. The most likely reason for this is, of course, that Sgr A* itself causes this potential well. One can use the assumption of equipartition of momentum between the fastest stars ($m_* v_*$) and Sgr A* ($M_{\mathrm{Sgr\,A^*}}\, v_{\mathrm{Sgr\,A^*}}$) to infer a lower limit on the mass of Sgr A* from the VLBI proper motion studies

$$M_{\mathrm{Sgr\,A*}} \gtrsim 1,000\, M_\odot \left(\frac{m_*}{10\, M_\odot}\right) \left(\frac{v_*}{1,500\,\mathrm{km/s}}\right) \left(\frac{v_{\mathrm{Sgr\,A*}}}{15\,\mathrm{km/s}}\right)^{-1}. \quad (11.7)$$

Numerical modeling of n-body interactions suggest that under most conditions this lower limit can be as high as $10^5 M_\odot$ (Reid et al. 1999). This mass is way beyond those of any stellar object and hence it is very reasonable to assume that essentially all the dark mass of $2-3\cdot 10^6 M_\odot$ is concentrated inside Sgr A*—the radio source.

11.2.4 Radio Spectrum of Sgr A*

A major input for modeling the nature of the central black hole candidate of our Galaxy is the emission spectrum. Typical luminous black holes, e.g. those in quasars, emit over a broad range in frequencies. In contrast, for Sgr A* only radio emission was reliably detected over many years, with the late addition of X-ray emission. One reason for this dimness is certainly the low accretion rate and quite plausibly the presence of a radiatively deficient accretion flow (Coker, this volume).

At frequencies below 1 GHz the spectrum is essentially undetermined. First of all, the scattering size of Sgr A* becomes larger than 1 arcsecond and the source starts to blend with its surroundings. Secondly, the Sgr A complex becomes optically thick at low frequencies (Pedlar et al. 1989) and Sgr A* may be obscured. It is also possible, but less likely, that the claimed low-frequency turnover in the spectrum (Davies, Walsh, & Booth 1976) has an intrinsic nature.

At higher frequencies the radio spectrum of Sgr A* has been measured with great accuracy in various campaigns up into the THz regime (e.g., Wright & Backer 1993, Zylka et al. 1995, Serabyn et al. 1997, Falcke et al. 1998). Since the source is variable (see Fig. 11.3), it is useful to consider either simultaneous or time-averaged spectra. Such an average spectrum is shown in Figure 11.7 compiled by Melia & Falcke (2001). The overall radio spectrum is slightly inverted, i.e. has a positive spectral index ($\alpha \simeq 0.2$, $S_\nu \propto \nu^\alpha$) in the GHz regime. The average radio flux density is around 1 Jy. At the highest radio frequency ($\gtrsim$ 100 GHz), the spectrum seems to become even more inverted until it abruptly cuts off somewhere in the far-infrared. This upturn and subsequent cut-off has been interpreted as an effect of the finite size of the central object with a size scale as expected for a $3 \cdot 10^6 M_\odot$ black hole (e.g., Falcke & Biermann 1994 and below). The up-turn in the spectrum at submm-wavelengths is often referred to as the "submm-bump".

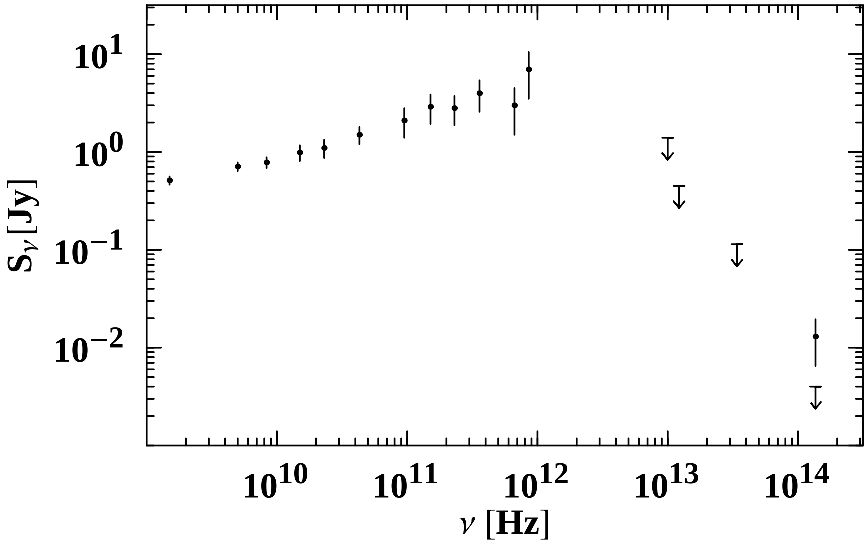

Figure 11.7 Time-averaged spectrum—flux density versus frequency—of Sgr A* from radio to the near-infrared as compiled by Melia & Falcke (2001). The error bars in the radio regime indicate variability (one standard deviation).

11.2.5 Polarization of Sgr A*

Finally, as a relatively recent development, the polarization properties of Sgr A* are now relatively well established. For a long time it was generally thought that, in marked contrast to more luminous AGN, Sgr A* is unpolarized. This is true for linear polarization in the GHz radio regime. Bower et al. (1999) found an upper limit of $\leq 0.1\%$ to the linear polarization at cm-waves, however, they found plenty of circular polarization.

The results for linear polarization at low frequencies were obtained with a rarely used technique in radio, called spectro-polarimetry. This allows one to look for polarization in small frequency bands. Usually in continuum observations one averages the polarization of the radiation over the available bandwidth $\delta\nu$. However, since Sgr A* may be embedded in a dense plasma, Faraday rotation in the accretion flow or a foreground

Galactic screen could lead to a rotation of the linear polarization vector even within the small bandwidth.

Faraday rotation is produced when radio waves pass through an ionized and magnetized medium. Since left and right circularly polarized waves have different refractive indices for a given magnetic field orientation, a wavelength-dependent delay is induced that rotates the position angle ϕ of the linear polarization vector by an amount

$$\Delta\phi = \mathrm{RM}\,\lambda^2. \tag{11.8}$$

The parameter RM is called the rotation measure and can be determined by measuring the position angle of the linear polarization vector ϕ at different wavelengths. For a given frequency bandwidth $\delta\nu$, significant depolarization is obtained if $\Delta\phi \sim 1$ rad. Hence, for a typical VLA bandwidth of $\Delta\nu = 50$ MHz at 4.8 GHz a rotation measure of RM$= 10^4$ rad m^{-2} of any foreground material would destroy any intrinsic polarization signal. Such a value for RM is large compared to what is seen in other AGN but cannot be excluded in the Galactic Center. By Fourier-transforming spectro-polarimetric data (to look for periodic signals due to a fast rotation of the polarization vector as a function of frequency), Bower et al. (1999) were able to set the 0.1% limit and also exclude rotation measures below RM$\lesssim 10^7$ rad m^{-2} as the cause for the low polarization.

Later, Aitken et al. (2000) made linear polarization observation with a single dish sub-millimeter wave telescopes and found $\sim$10% linear polarization above 150 GHz. This was confirmed with an interferometer by Bower et al. (2002b) and they also found evidence for a large rotation measure $\lesssim 10^6$ rad m$^-2$ plus some evidence for intrinsic depolarization towards lower frequencies. At the moment of writing this is a strongly developing field which promises many new insights in the future. For example, one can use the measured RM to limit the accreting material engulfing Sgr A* (Agol 2000).

As a big surprise, Bower, Falcke, & Backer (1999) also found strong circular polarization at the 0.3-1% level. This is unusual because typical AGN have more linear than circular polarization and it can be used to constrain the electron content and distribution in Sgr A* (see Sec. 11.3.4). Interestingly, the circular polarization turned out to be variable itself. At higher frequencies the variability as well as the fractional polarization increase (Bower et al. 2002a). Figure 11.8 shows a summary of the currently known polarization properties of the Sgr A* spectrum.

11.3 Radio and X-ray Emission from a Black Hole Jet

A very common feature of active black holes in the radio regime is the compact radio core with its characteristic, flat spectrum. In luminous quasars

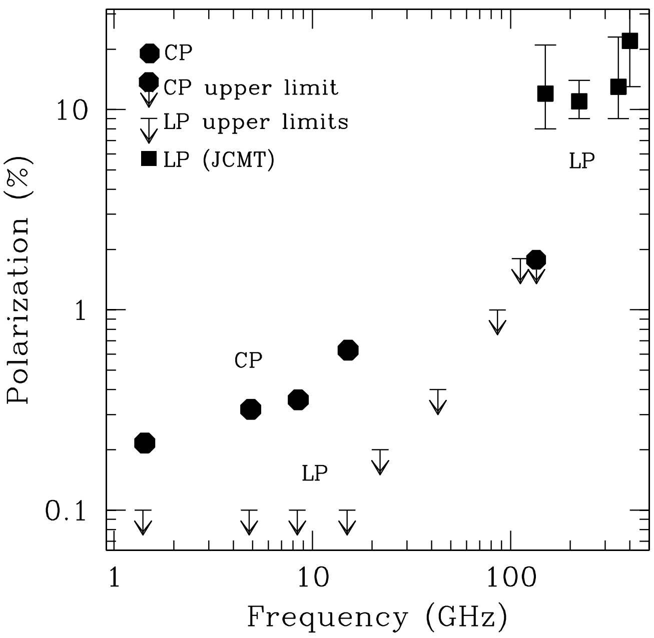

Figure 11.8 The average fractional circular polarization of Sgr A* and upper limits to the linear polarization from Bower et al. (2002; and references therein). In the top right corner we show the linear polarization values given in Aitken et al. (2000) from single dish values. The error bars are 1σ errors.

the cores are known for many years. Studying these radio cores with VLBI has allowed us to make the most detailed images of the physics and environment of black holes (Zensus 1997). Such flat-spectrum radio cores have also been found in many nearby galaxies which show signs of nuclear activity (Wrobel & Heeschen 1984, Nagar et al. 2000, Falcke et al. 2000). A well studied example is M81*, the compact core in the nearby galaxy M81, which shares many characteristics with Sgr A* (Reuter & Lesch 1996, Bietenholz, Bartel, & Rupen 2000, Brunthaler et al. 2001). In essentially all cases these cores are related to relativistic outflows or jets. For that reason, we start with the most simple-minded assumption, namely that Sgr A* is not very different either and we will discuss in the following how to obtain the observed radio spectra within the context of jet physics.

11.3.1 The Flat Radio Spectrum

The fact, that flat radio spectra for radio cores are so ubiquitous, suggests that this is a very robust feature that must arise naturally. This is indeed the case for initially collimated, then freely expanding, supersonic radio plasmas. Why is this so?

Let us consider a plasma jet ejected from the vicinity of the black hole. Mechanisms for this collimated launching of jets have been discussed in the literature (see, e.g., Ferrari 1998 and references therein) and are mostly magneto-hydrodynamic (MHD) in origin. Observationally, jets span an enormous range of spatial scales — from milliparsecs to Megaparsecs — and maintain their basic structure for long stretches (see, e.g., Bridle & Perley 1984, Fig. 2). Here, we consider the part, where the jet has left the acceleration and collimation region and is essentially in a free expansion. If the jet has not yet propagated and expanded too far, it is usually a good assumption to assume that the jet is highly over-pressured with respect to the external medium. We use a cylindrical coordinate system where z is along the jet axis and r is perpendicular to it.

Let us assume the jet plasma moves in the forward direction with a relativistic and almost constant proper velocity (bulk speed)

$$v_{\mathrm{z}} = \gamma_{\mathrm{j}}\beta_{\mathrm{j}}c, \tag{11.9}$$

along the jet axis. The sideways expansion will happen with the respective sound velocity

$$v_{\mathrm{s}} = \gamma_{\mathrm{s}}\beta_{\mathrm{s}}c, \tag{11.10}$$

if we can ignore the external pressure and we are well beyond the sonic point where we can neglect adiabatic losses.

Here we use the well known definition of the relativistic Lorentz factor and the dimensionless velocity,

$$\gamma = \sqrt{\frac{1}{1-\beta}} \quad \text{and} \quad \beta = \frac{v}{c}. \tag{11.11}$$

With longitudinal and lateral expansion being of constant velocity the plasma will expand into a cone of half opening angle

$$\phi \simeq \frac{1}{\mathcal{M}} \quad \mathcal{M} = \frac{\gamma_{\mathrm{j}}\beta_{\mathrm{j}}}{\gamma_{\mathrm{s}}\beta_{\mathrm{s}}}, \tag{11.12}$$

where $\mathcal{M}$ is the relativistic Mach number (see Königl 1980). The shape is given by

$$r = \frac{z}{\mathcal{M}}. \tag{11.13}$$

This naturally resulting conical structure is the basis for the self-similar structure of jets.

The scaling of the relevant parameters for calculating the synchrotron emission, electron density n_{e}, and magnetic field B, can be obtained from simple conservation laws. First, we demand that the particle number N_e is conserved along the flow and set the total mass flux to

$$\dot{M}_j = \frac{d(m_p N_e)}{dt} = \rho v_z A = \text{const.} \tag{11.14}$$

Note that the total mass flux is determined by the protons in the fully ionized plasma and we assume charge balance between electrons and protons ($N_e = N_p$); ρ is the mass density and $A = \pi r^2$ the cross section of the jet. The particle density n_e is then given by

$$n_e(r) = \frac{\dot{M}_j}{m_p \cdot \gamma_j \beta_j c \cdot \pi r^2} \propto r^{-2}. \tag{11.15}$$

We can use the same argument to get the scaling for the magnetic field, by demanding that the comoving magnetic field energy in a turbulent plasma is conserved:

$$\dot{E}_B = L_B = \rho_B v_z A = \text{const.} \tag{11.16}$$

Here we use L_B as a measure for the magnetic power fed into the jet. The energy density of the magnetic field is given by

$$\rho_B = B_j^2/8\pi \tag{11.17}$$

and consequently we get

$$B_j(r) = \sqrt{\frac{8L_B}{\gamma_j \beta_j c \cdot r^2}} = 36\,\text{G}\ (\gamma_j\beta_j)^{-1/2} \left(\frac{L_B}{1000 L_\odot}\right)^{1/2} \left(\frac{r}{R_s}\right)^{-1} \propto r^{-1}, \tag{11.18}$$

where for the Galactic Center we have a Schwarzschild radius of

$$R_s = \frac{2GM_\bullet}{c^2} = 0.9 \cdot 10^{12}\,\text{cm} \left(\frac{M_\bullet}{3 \cdot 10^6 M\odot}\right). \tag{11.19}$$

Of course, this implies that the energy content in magnetic field and relativistic particles remains a fixed ratio throughout the jet. One therefore relates these two crucial parameters of a jet by an “equipartition relation” such that the total energy in particles is a fraction k of the total energy in the magnetic field. For simplicity we assume that all electrons are of the same energy $E_e = \gamma_e m_e c^2$, with γ_e being the electron Lorentz factor characterizing the internal energy or temperature of the electrons (not to be confused with the bulk Lorentz factor of the entire flow)[3]. We can equate the energy densities,

[3] The results will not be very different for a thermal distribution of electrons or a power-law distribution with a low-energy cut-off around γ_e

$$n_{\rm e}\gamma m_{\rm e}c^2 = k\frac{B^2}{8\pi}, \text{ and yield } n_{\rm e} = \frac{kB^2}{8\pi\gamma m_{\rm e}c^2}. \tag{11.20}$$

Here we only consider the internal energy of the jet. The total energy of the jet will of course be still dominated by the kinetic energy of the protons – but not by a huge factor. A proper discussion of the *total* energy budget requires solution of the relativistic Bernoulli equation and is discussed in Falcke & Biermann (1995).

To calculate the radio emission, we need to know the scaling of the synchrotron emission and absorption coefficients. This can be obtained, e.g. from Pacholczyk (1970; Eqs. 3.43 & 3.44) for electrons with a pitch angle $\alpha_{\rm e}$ with respect to the magnetic field. The emission and absorption coefficients are respectively

$$\epsilon_\nu = n_{\rm e}\cdot\frac{\sqrt{3}e^3}{4\pi m_{\rm e}c^2}B\sin\alpha_{\rm e}\cdot F\left(\frac{\nu}{\nu_{\rm c}}\right), \tag{11.21}$$

and

$$\alpha_\nu = n_{\rm e}\cdot c^2\sqrt{\frac{3e}{4\pi m_{\rm e}^3c^5}}\frac{\sqrt{3}e^3}{4\pi m_{\rm e}c^2}\left(B\sin\alpha_{\rm e}\right)^{3/2}\nu_{\rm c}^{-5/2}K_{5/3}\left(\frac{\nu}{\nu_{\rm c}}\right), \tag{11.22}$$

with

$$\nu_{\rm c} = \frac{3\gamma_{\rm e}^2 e}{4\pi m_{\rm e}c}B\sin\alpha_{\rm e}. \tag{11.23}$$

$F(x)$ is a function with asymptotic limit $F(x)\sim\frac{4\pi}{\sqrt{3}\Gamma(1/3)}\left(\frac{x}{2}\right)^{1/3}$ for $x\ll 1$ which has a maximum at

$$\nu_{\rm max} = 0.29\nu_{\rm c}. \tag{11.24}$$

$K_{5/3}(x)$ is the Bessel K function which can be Taylor expanded into $K_{5/3}(x) = 1.43x^{-5/3}$ for $x << 1$. For the pitch angle we can take an average value:

$$\langle\alpha_{\rm e}\rangle = \arcsin\left(\frac{\int_0^{\pi/2}\sin\alpha\sin\alpha\; d\alpha}{\int_0^{\pi/2}\sin\alpha\; d\alpha}\right)\simeq 52^\circ. \tag{11.25}$$

Using the asymptotic behavior and average pitch angle, we can evaluate emission and absorption coefficients and obtain handy approximate formulae:

$$\epsilon_\nu = 6.0\cdot 10^{-20}\,{\rm erg\,s^{-1}\,Hz^{-1}cm^{-3}}\; k\left(\frac{B}{\rm Gauss}\right)^{8/3}\left(\frac{\gamma_{\rm e}}{100}\right)^{-5/3}\left(\frac{\nu}{\rm GHz}\right)^{1/3} \tag{11.26}$$

and

$$\alpha_\nu = 3.5\,10^{-14}\,\mathrm{cm}^{-1}\;k\left(\frac{B}{\mathrm{Gauss}}\right)^{8/3}\left(\frac{\gamma_{\mathrm{e}}}{100}\right)^{-8/3}\left(\frac{\nu}{\mathrm{GHz}}\right)^{-5/3}. \qquad (11.27)$$

The synchrotron spectrum of a mono-energetic electron distribution will have a characteristic shape consisting of three parts: a) an optically thick spectrum with $S_\nu \propto \nu^2$ at frequencies $\nu \ll \nu_{\mathrm{ssa}}$ below the self-absorption frequency, b) an optically thin spectrum with $S_\nu \propto \nu^{1/3}$ at intermediate frequencies $\nu_{\mathrm{ssa}} < \nu < \nu_{\mathrm{c}}$, and c) an exponential high-frequency cut-off beyond $\nu \gg \nu_{\mathrm{c}}$. In most realistic cases for jets the intermediate region will not assume the $\nu^{1/3}$-law, since ν_{c} and ν_{ssa} are close together leading to a curved spectrum.

The self-absorption frequency can be calculated from Eq. 11.27 and Eq. 11.18, by requiring that the optical depth through the jet, seen under an angle of $\theta \gg \mathcal{M}^{-1}$ from the jet axis, is unity:

$$\tau \sin^{-1}\theta R\alpha_\nu = 1. \qquad (11.28)$$

We find

$$\nu_{\mathrm{ssa}} = 2.3\,\mathrm{GHz}\;k^{3/5}\sin^{-3/5}\theta\,(\gamma_{\mathrm{j}}\beta_{\mathrm{j}})^{-4/5}\left(\frac{\gamma_{\mathrm{e}}}{100}\right)^{-8/5}\left(\frac{L_{\mathrm{B}}}{1000L_\odot}\right)^{4/5}\left(\frac{R}{\mathrm{AU}}\right)^{-1}. \qquad (11.29)$$

The maximum flux of synchrotron emission is found at a frequency of $\nu_{\mathrm{max}} = 0.29\nu_{\mathrm{c}}$ (Eq. 11.24; see also Rybicki & Lightman 1979, Fig. 6.6). Using Eqs. 11.23 & 11.18 we find

$$\nu_{\mathrm{max}} = 21\,\mathrm{GHz}\;(\gamma_{\mathrm{j}}\beta_{\mathrm{j}})^{-1/2}\left(\frac{\gamma_{\mathrm{e}}}{100}\right)^{2}\left(\frac{L_{\mathrm{B}}}{1000L_\odot}\right)^{1/2}\left(\frac{R}{\mathrm{AU}}\right)^{-1}. \qquad (11.30)$$

As one can see, and as hinted at above, both frequencies are within an order of magnitude for near-equipartition situations and both scale with $R^{-1} = (Z/\mathcal{M})^{-1}$ (Eq. 11.13).

Since the synchrotron spectrum peaks near these frequencies one also sees that for a given observing frequency the maximum of emission in the spatial domain will be at one characteristic zone in the jet. A different observing frequency will reveal a different maximum. This effect produces a core shift that is well known in quasar jets. Since the size of the emitting region, $\Delta R \simeq Z/\mathcal{M}$ will be proportional to the distance one also expects a different core-size for different frequencies:

$$Z_{\mathrm{max}} = 21\,\mathrm{AU}\;\mathcal{M}\,(\gamma_{\mathrm{j}}\beta_{\mathrm{j}})^{-1/2}\left(\frac{\gamma_{\mathrm{e}}}{100}\right)^{2}\left(\frac{L_{\mathrm{B}}}{1000L_\odot}\right)^{1/2}\left(\frac{\nu}{\mathrm{GHz}}\right)^{-1}. \qquad (11.31)$$

The effect of a roughly ν^{-1} core size was also nicely demonstrated by Bietenholz, Bartel, & Rupen (2000) for M81*. For Sgr A* this effect is not visible at cm-waves due to the frequency-dependence of the scatter broadening.

At the Galactic Center distance of $D = 8$ kpc, 1 AU corresponds to 0.125 mas. For comparison, the claimed size for Sgr A* at 43 GHz by Lo et al. (1998) was $\lesssim$0.7 mas. Equation 11.31 predicts a shift of order 0.25 mas$\cdot\,(\mathcal{M}/4)\,(L_{\rm B}/1000L_\odot)$ at 43 GHz.

Another useful comparison is the maximum frequency of the entire spectrum. For the smallest size of the system, one Schwarzschild radius $R_{\rm s} = 0.9\cdot 10^{12}$ cm $= 0.06$ AU, we find a maximum frequency of $\sim$350 GHz from Eq. 11.30. Hence it is immediately understandable, why the Sgr A* spectrum has to turn over at higher frequencies, beyond the submm-bump. In this respect the location of the submm-bump is a rough indicator of the size of the black hole in the Galactic Center.

Finally, we can calculate the total spectrum. We know that each frequency is dominated by a relatively small spatial region $Z(\nu)$ in the jet at the scale given by equation 11.31. The volume of this region can be approximated by a cylinder, $V = \pi R^2 Z$, where R is given by Eq. 11.13. This volume has to be multiplied by the emission coefficient (Eq. 11.26) with the magnetic field (Eq. 11.18) inserted. Divided by the surface of an imaginary absorbing sphere at the observers distance D, we get the flux density of the jet as a function of frequency:

$$\begin{aligned} S_\nu &= \epsilon_\nu(\nu_{\rm c})\frac{\pi R^2 Z}{4\pi D^2} \\ &= 1.0{\rm Jy}\, k\frac{\mathcal{M}}{4}\left(\frac{\gamma_{\rm e}}{100}\right)^{-1}(\beta_{\rm j}\gamma_{\rm j})^{-3/2}\left(\frac{L_{\rm B}}{1000L_\odot}\right)^{3/2}. \end{aligned} \tag{11.32}$$

As we can see, the frequency cancels out thus implying a perfectly flat spectrum ($S\nu \propto \nu^0$). This is a fairly general result that applies to essentially all flat-spectrum radio cores in black hole jets. A schematic view of how the flat spectrum arises is also shown below in Figure 11.9.

The equations have all been normalized by a magnetic luminosity of $L_{\rm B} \simeq 1000L_\odot$. Of course, the jet has also other energetic components (e.g., turbulence or cold protons), however, for a maximally efficient jet they will be of similar order (Falcke & Biermann 1995).

The total energy content of the jet will therefore be a few times higher, i.e. of order 10^{37} erg sec^{-1}. Assuming the efficiency for the jet production is of order of $0.1\dot{M}c^2$ (e.g., Falcke, Malkan, & Biermann 1995) this would require an accretion rate of at least $\gtrsim 2\cdot 10^{-9} M_\odot$ yr^{-1} onto Sgr A*. This is quite in the range of – and sometimes well below – the accretion rates discussed for Sgr A*.

In our derivation we have so far completely ignored relativistic effects on the emitted spectrum. For a continuous relativistic jet where $\beta_{\rm j} \simeq 1$ and $\gamma_{\rm j} \gg 1$, relativistic beaming will lead to a modification of the observed spectrum (Lind & Blandford 1985) by

$$S'_\nu = \mathcal{D}^2 S_\nu \quad \& \quad \nu' = \mathcal{D}\nu, \tag{11.33}$$

where one defines the relativistic Doppler factor as

$$\mathcal{D} = \frac{1}{\gamma_{\rm j}\,(1-\beta_{\rm j}\cos\theta)}. \tag{11.34}$$

For moderate inclination angles and moderate jet velocities the effect will be of order unity and we have neglected this for the sake of clarity. From this simple exercise we can conclude that the basic properties of Sgr A*, spectrum, flux, and size, can be naturally reproduced by a jet model.

For a more realistic model, one has to take several additional effects into account. For example, we have here assumed a constant velocity of the jet. This is somewhat inconsistent, since the jet as presented here has a pressure gradient that will naturally lead to some mild acceleration of the jet plasma along the jet axis. This effect together with the relativistic corrections will lead to a slightly inverted radio spectrum and a slightly smaller exponent for the size-frequency relation (Falcke 1996a).

In addition we have not yet yet dealt with the submm-bump in the spectrum. From Eqs. 11.30 & 11.31 it is clear that this emission has to come from the innermost region of the jet (the "nozzle"; Falcke 1996b) or the inner edge of the accretion flow (Melia, Liu, & Coker 2000, Narayan et al. 1998). A simple descriptive calculation to estimate the parameters of this region, which follows essentially the procedure outline here, is given in (Melia & Falcke 2001, Sec. 5.2).

All these effects including the X-ray spectrum are dealt with in more sophisticated numerical calculation which are are discussed in the next sections.

11.3.2 The X-ray Spectrum

After having calculated the radio spectrum, we can now make a rough estimate of the expected X-ray spectrum from Sgr A*. For AGN, there are typically four processes discussed to explain the observed X-ray emission in various objects: a) synchrotron emission, b) Bremsstrahlung, c) thermal Comptonization by a hot corona, d) inverse Compton scattering of photon off the relativistic electrons in the jet plasma. Possibility a) can be excluded here since the radio synchrotron spectrum cuts off already in the mid-infrared, b) and c) have been discussed by Coker (this volume). Thus, we will here concentrate on the fourth possibility.

Since the only photons we see from Sgr A* outside the X-ray regime are radio photons, we will here consider solely the synchrotron self-Compton (SSC) process, which is absolutely unavoidable. The relativistic electrons that produce synchrotron radiation also have a finite probability to Compton up-scatter the very photons they have produced in the first place. The frequency of the up-scattered photons will be increased by a factor $\simeq \gamma^2$ with respect to the target photons. Inverse-Compton is a scattering process, where the probability of an interaction of an electron from a population with particle density $n_{\rm e}$ with a photon of a population with photon density n_γ depends on $n_{\rm e} \cdot n_\gamma$. Since in SSC the electrons are also responsible for the target photons, the efficiency of SSC will go as $n_{\rm e}^2$. For the case of a jet, where the density increases inwards with R^{-2}, while the volume decreases inwards with R^3, the dominant contribution to the up-scattered spectrum will be at the smallest scale in the system, where $n_{\rm e}$ is maximal. Following the previous discussion, this will be at a few Schwarzschild radii where the submm-bump in the spectrum is produced.

One can show (Rybicki & Lightman 1979, Sec. 7.2) that the luminosity $L_{\rm SSC}$ of the inverse-Compton process is proportional to the luminosity of the synchrotron emission $L_{\rm sync}$, with the proportionality factor given by the ratio of the energy densities in synchrotron photons

$$U_{\rm ph} = \frac{L_{\rm sync}}{4\pi R^2 c} \tag{11.35}$$

and magnetic field

$$U_{\rm B} = B^2/8\pi, \tag{11.36}$$

such that

$$L_{\rm SSC} = \frac{U_{\rm ph}}{U_{\rm B}} L_{\rm sync}. \tag{11.37}$$

From Fig. 11.7 we find that the maximum of emission in Sgr A* is about 3 Jy at 10^{12} Hz. Hence the synchrotron luminosity of Sgr A* is

$$L_{\rm sync} = 2.3 \cdot 10^{35}\,\frac{\rm erg}{\rm s}\,\left(\frac{S_\nu}{\rm 3Jy}\right)\left(\frac{D}{\rm 8kpc}\right)^2\left(\frac{\nu_{\rm max}}{10^{12}{\rm Hz}}\right) \tag{11.38}$$

and from Eqs. 11.18 and 11.37 we get, independent of the radius,

$$L_{\rm SSC} = 3.4 \cdot 10^{33}\,\frac{\rm erg}{\rm s}\,(\beta_{\rm j}\gamma_{\rm j})\left(\frac{S_\nu}{\rm 3\,Jy}\right)^2\left(\frac{D}{\rm 8kpc}\right)^4\left(\frac{\nu_{\rm max}}{10^{12}{\rm Hz}}\right)^2\left(\frac{L_{\rm B}}{1000L_\odot}\right)^{-1}. \tag{11.39}$$

As one can see the SSC emission is sensitive to the ratio between synchrotron emission and magnetic field. Using a different parameterization this gives one a dependence on the equipartition factor k. In general one can also state that the SSC emission should be more variable than the synchrotron emission since it depends with a high power on flux density and peak synchrotron frequency.

The peak of the SSC emission itself will be roughly at $\gamma^2 \cdot \nu_{\rm max}$. For $\gamma_{\rm e} \simeq 100$ and $\nu_{\rm max} \simeq 10^{12}$ Hz the peak will be above 10^{16} eV, hence in the far ultraviolet and soft X-rays.

All of this is quite consistent with the X-ray observations by Baganoff et al. (2001) who find a quiescent, soft X-ray emission of a few times 10^{33} erg sec^{-1} in Sgr A* which can be rapidly variable at times.

A schematic view of how the spectrum of Sgr A* from radio to X-rays can be composed from the various parts discussed here is shown in Figure 11.9.

11.3.3 Numerical Results

After we have verified, that the basic properties of Sgr A* can be explained with a synchrotron+SSC jet model, we can consider a more sophisticated numerical approach. This has been outlined in Falcke & Markoff (2000), Markoff et al. (2001), and Yuan, Markoff, & Falcke (2002).

We start with the basic jet emission model (Falcke & Biermann 1999, Falcke & Markoff 2000), consisting of a conical jet with pressure gradient, nozzle and relativistic effects. The parameters in the nozzle for the quiescent state are determined from the underlying accretion disk, assumed to be an ADAF, as described in Yuan, Markoff, & Falcke (2002). All quantities further out in the jet are solved for using conservation of mass and energy, and the Euler equation for the accelerating velocity field. The results are shown in Figs. 11.10 & 11.11 and show that the model is able to reproduce the observed spectrum and size in detail.

11.3.4 The Circular Polarization

Finally, for understanding the radio properties we also have to consider the surprising results of the polarization observations, where a relatively large circular polarization (CP) was found. The following intuitive explanation is essentially a discussion of CP based on the paper by Beckert & Falcke (2002), where one can find more details. The main point is that linear polarization is naturally obtained in synchrotron radiation (up to 70% for homogeneous magnetic fields), while CP is strongly suppressed in synchrotron plasmas with $\gamma_{\rm e} \gg 1$. The reason for this is that the narrow beaming cone of the relativistic electron allows one to see only a small arc along the gyration around the magnetic field. However, CP can be obtained through radiation transfer, particularly through the fact that a magnetic plasma will naturally be bi-refringent.

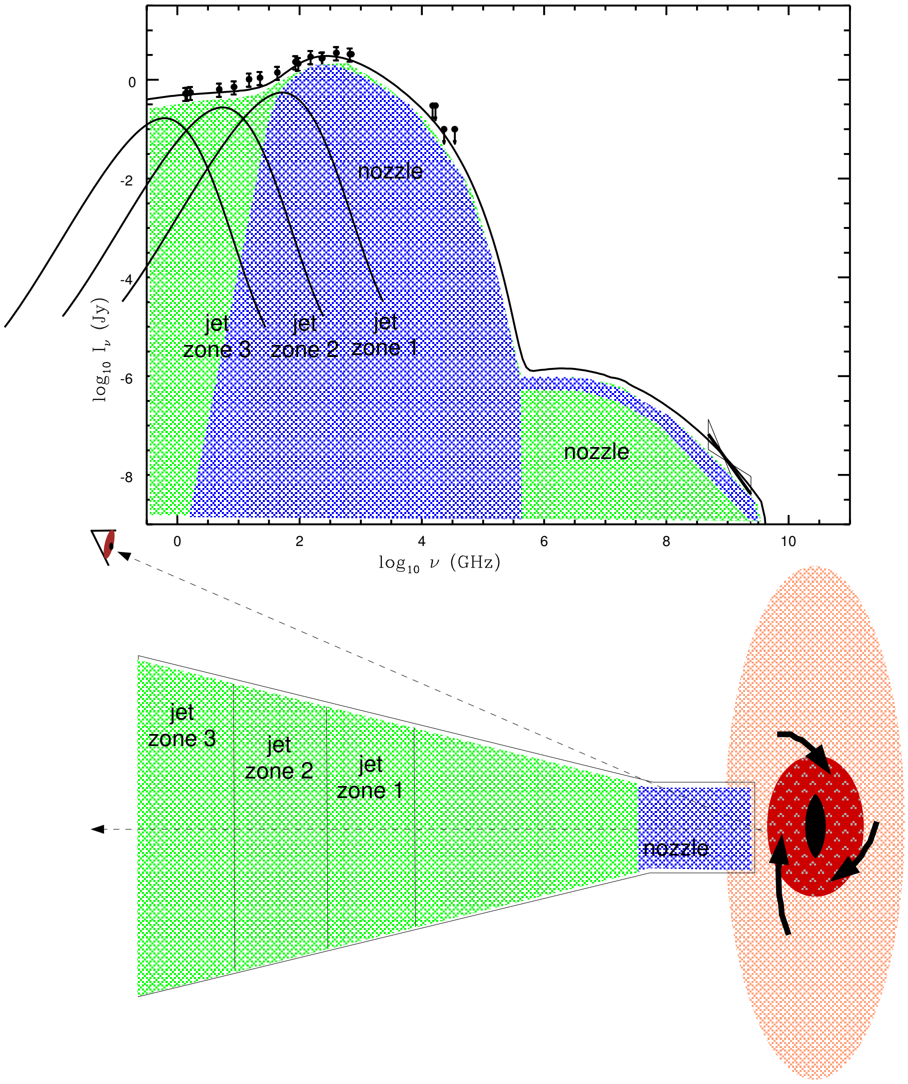

Figure 11.9 This is a schematic of the jet model. The accretion disk/flow is assumed to be radiatively unimportant. The submm-bump and the X-ray emission are produced by the jet nozzle region. The flat part of the radio spectrum is the sum of individual, peaked synchrotron spectra from increasingly distant zones in the jet. The peak frequency of each of these spectra shifts to lower frequencies as one goes out, while the peak flux density stays essentially at the same level or decreases only slowly. Figure from S. Markoff, based on Falcke & Markoff (2000).

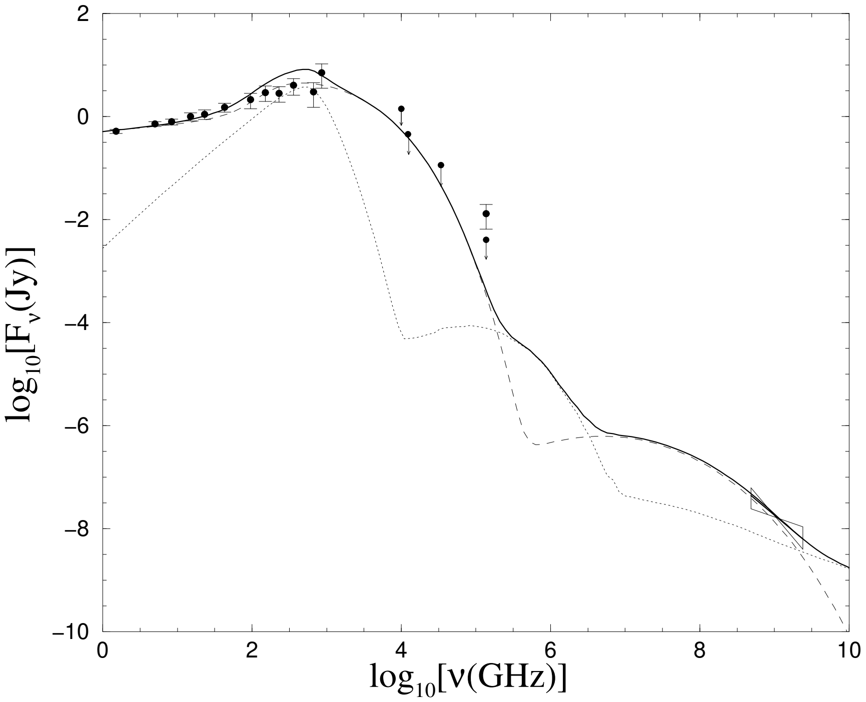

Figure 11.10 The jet-disk spectral model for Sgr A*. The dotted line is for the ADAF (optically thin, advection dominated accretion flow) contribution, the dashed line is for the jet emission, and the solid line shows their sum. For the most part, the emission is dominated by the jet-spectrum. The submm-bump is produced by the jet nozzle with a possible contribution from the accretion flow. The X-ray emission is largely SSC emission from the nozzle with a slight contribution from more extended thermal X-ray emission from the accretion flow. We have here assumed an accretion rate of $10^{-6} M_\odot$ yr^{-1}, where only 0.1% of the power goes into the jet. For a 10% efficiency the required accretion rate is about $10^{-8} M_\odot$ yr^{-1} and the disk contribution would be negligible. The model is discussed in more detail in Yuan et al. (2002).

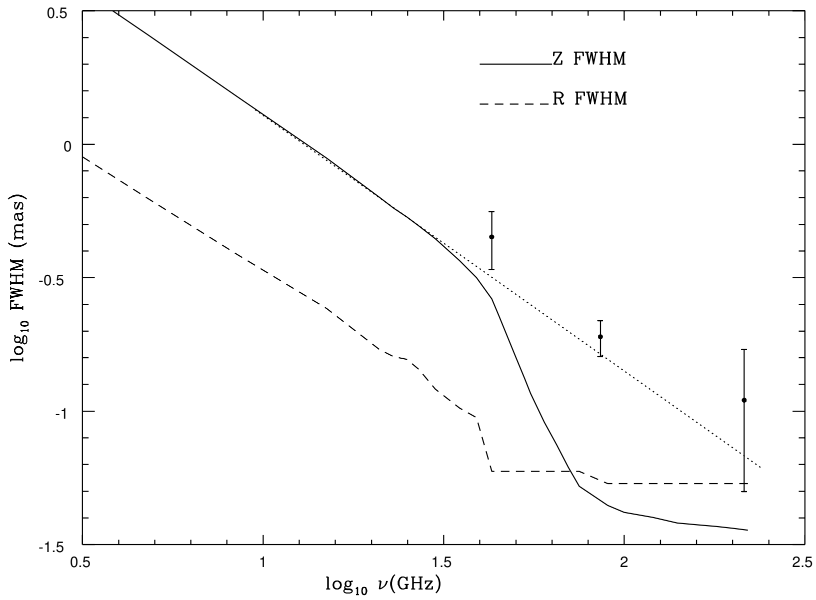

Figure 11.11 Projected size of the major and minor axis of the jet in Sgr A* as a function of frequency. The filled dots mark the size as measured by Lo et al. (1998; 43 GHz) and Krichbaum et al. (1998; 86 & 215 GHz). The lines represent the predictions of the jet model. At frequencies above 30 GHz one obtains a two component structure with an increasingly stronger core (nozzle, solid dashed line) and a fainter jet component (dotted line).

For simplicity let us now separate Faraday rotation from conversion and only picture purely linearly or circularly polarized waves in a homogeneous magnetic field.

The two orthogonal normal modes for propagation perpendicular to the magnetic field are linearly polarized and a purely circularly polarized wave is split into the two normal modes with a relative phase shift as shown in Fig. 11.12 (left). Without a phase-shift the wave will be purely linearly polarized. If, for example, a locally homogeneous magnetic field vertically pervades the box in Fig. 11.12 (left) along the z-direction, electrons or positrons will be free to move along the field lines and resonate with the vertical mode but hardly resonate with the horizontal mode along the x-direction. This yields the bi-refringence discussed above. The resonating electrons or positrons will themselves act as antennas and emit a somewhat delayed wave that interferes with the incoming vertical mode, leading to a slight phase-shift between vertical and horizontal mode. The effect of this

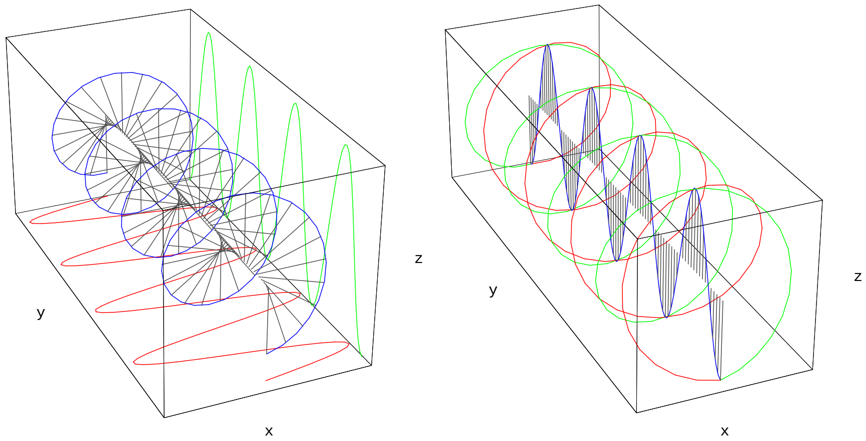

Figure 11.12 *Left:* A circularly polarized wave can be composed of two orthogonal linearly polarized modes shifted in phase. A phase shift would be produced by a plasma in a magnetic field perpendicular to the propagation direction of the waves (here along the z-direction). Without phase-shift the sum of the two modes would be a purely linearly polarized wave. The accompanying movie shows the effect of how phase-shifts in a region will turn such a linearly polarized wave into a circularly polarized wave (conversion).
Right: A linearly polarized wave can be composed of two orthogonal circularly polarized modes shifted in phase. A phase shift would be produced by a plasma in a magnetic field along the propagation direction of the waves (here along the y-direction). The accompanying movie shows the effect of additional phase-shifts on the linear polarization, leading to Faraday rotation.
The movies can be found at http://www.mpifr-bonn.mpg.de/staff/hfalcke/CP.

shift is shown in the accompanying animation[4], where the resulting wave is circularly polarized and switches from linear to circular polarization as a function of the shift.

Conversion acts also on initially only linearly polarized radiation. The amount of this conversion will depend on the misalignment between the incoming wave and the magnetic field direction since, obviously, a phase-shift between two orthogonal modes will have little effect if one mode is very small or non-existent. Moreover, a random distribution of magnetic field lines on the plane of the sky will reduce circular polarization from conversion in exactly the same way as linear polarization would be reduced.

[4] http://www.mpifr-bonn.mpg.de/staff/hfalcke/CP

Analogous to the picture for conversion, one can view a linearly polarized wave as composed of two circularly polarized normal modes when propagating along the magnetic field. This is sketched in Fig. 11.12 (right), where we will assume a longitudinal magnetic field, i.e. a field along the y-direction. The circular modes will resonate with either electrons or positrons gyrating around the magnetic fields. The latter will again emit a circularly polarized wave, producing a phase-shift when interfering with the incoming wave. The effect of the phase-shift in the circular modes is shown in the accompanying animation of Fig. 11.12 (right), where one can see that the resulting linearly polarized wave is simply (Faraday) rotated.

An important conclusion to remember therefore is, that conversion is mainly produced by magnetic field components perpendicular to the line-of-sight or photon direction, while Faraday rotation is produced by magnetic field components along the line-of-sight. Moreover, one can also see that conversion is insensitive to the electron/positron ratio while Faraday rotation is not. In Fig. 11.12 (left) an electron and an positron are both free to move along the z-axis. While they will respond in opposite directions to the incoming wave, their respective emitted waves will also have opposite signs because of opposite charges and hence be identical. In the case of Faraday rotation, the incoming left- or right-handed circularly polarized wave will only resonate with the particle that also has the correct handedness in its gyration – either electron or positron depending on the magnetic field polarity. A pure pair plasma would therefore produce exactly the same phase shift in left- and right-handed modes and not produce any net Faraday rotation. In the case of a charge-excess, the direction of Faraday rotation depends on the sign of the charge-excess (presumably electrons) and the polarity of the magnetic field. This will indirectly also affect the sign of circular polarization, if Faraday rotation is the ultimate cause of the misalignment between the plane of polarization and the magnetic field direction.

One can include these effects on the polarization into a radiation transfer code and try to reproduce the Sgr A* spectrum and polarization with a jet/outflow model (Beckert & Falcke 2002). The results are shown in Fig. 11.13 and nicely reproduce the observed spectrum. Two major conclusion can be drawn from this approach:

a) Since conversion is most effective for low-energy electrons one can conclude that a larger number of these low-energy electrons ($1 < \gamma_{\rm e} \ll 100$) are present in Sgr A*. In fact, in the specific modeling mentioned here, one finds that up to a factor of 100 more low-energy electrons could be present then the 'hot' electrons with $\gamma_{\rm e} \simeq 100$ invoked above to explain the spectrum. Hence, a large fraction of Sgr A*'s plasma could reside in a rather inconspicuous, "cold" and non-radiating (hidden) plasma.

b) Since the conversion requires an asymmetric magnetic field polarity, an outflow model with a helical magnetic field is strongly favored. The stability of the sign of CP also suggests that the polarity (the North pole of the black hole/jet) remains stable over some 20 years — a long time scale compared to the accretion time in optically thin accretion flows. It is possible that this stable polarity reflects the stable polarity of the Galactic magnetic field pervading the central parsec of the Galaxy which is accreted onto the black hole.

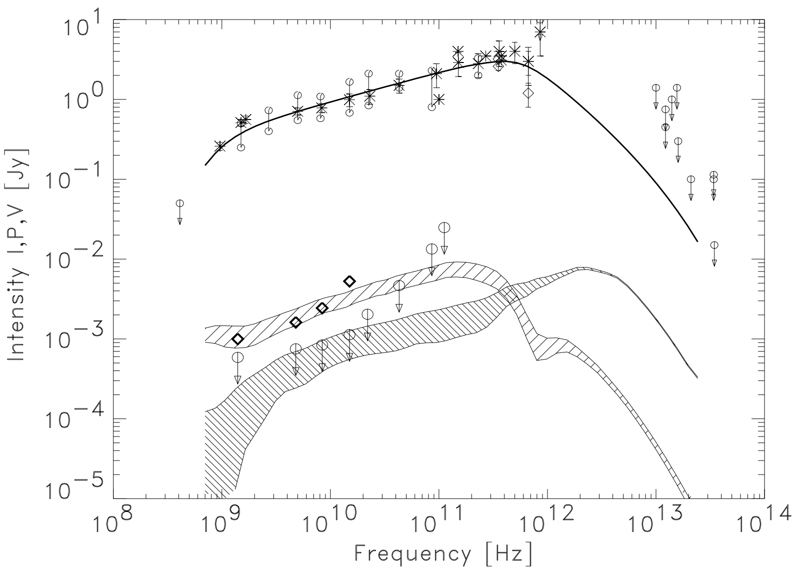

Figure 11.13 Outflow model for the radio spectrum of Sgr A* with polarization. The result of model calculations for total flux I (solid line), linearly polarized P (dense shaded area), and circularly polarized flux V (sparse area) are shown for a distance of 8 kpc. Diamonds show the observed circular polarization and circles the observed linear polarization, the rest are observed total flux density values. The numerical calculations are based on the model described in Beckert & Falcke (2002). The shaded areas mark the expected variability due to turbulence. The global magnetic field structure is a spiral with $B_\phi/B_z = 1$.

The main uncertainty in the modeling of the polarization at present reflects the uncertainty in what suppresses the linear polarization in Sgr A*. Here, we have simply assumed that the de-polarization of the linear polarization is due to intrinsic Faraday de-polarization in the radio source itself. However, this could similarly be done in a "foreground" screen, which would most likely be associated with the accretion flow. If that is the case, some of the "hidden matter" mentioned above would be in the actual accretion flow and not in the outflow/jet. This can be used to constrain the accretion rate. Estimates by Agol (2000) and Quataert & Gruzinov (2000) then yield a limit on the accretion flow of $\dot{M} \lesssim 10^{-8}$ to $10^{-9} M_{\odot}\ \mathrm{yr}^{-1}$, given the rotation measures inferred from the linear polarization observations at λ1mm.

11.3.5 Comparison with Other Supermassive Black Holes

An important input factor to the model discussed so far is the power of the jet (here we mainly considered the magnetic power L_{B}). A nice feature of the model is that it can be scaled over many orders of magnitude by just changing the power input of the jet. This is presumably done by a parallel change in the accretion disk power. Doing so would change the power of the radio core but would not change its spectral shape — only the turnover frequency might change. To a radio observer the jet would always appear as a flat-spectrum core. This may be the reason why radio jets are expected in almost every type of active black holes: from supermassive to stellar, from powerful to faint.

Indeed, compact, flat-spectrum radio cores have been found in sources like Quasars, Seyfert galaxies, Low-Luminosity AGN and LINERs, as well as in X-ray binaries, confirming that the physics we have discussed for Sgr A* are fairly universal. The exact nature of the cores and the emission of these other engines is not the main focus of the book and further discussion of this point can be found in Falcke (2001). However, the general point one can make is that as the accretion power and the disk luminosity decreases, one expects to see fainter radio cores. If there is a range in accretion rates throughout the universe, we also expect a range of core luminosities. This is demonstrated in Fig. 11.14, where Sgr A*-like radio cores of various different types are shown for a range of luminosities. In such a plot, Sgr A* would come in a the bottom left of the distribution for an accretion rate of $\simeq 10^{-8} M_{\odot}\ \mathrm{yr}^{-1}$ (as indicated by the upper black dot with horizontal error bar; the other point indicates the estimated position for M31* — the core in the Andromeda galaxy). However, since the accretion disk in Sgr A* is so faint and the accretion rate so uncertain, we cannot actually derive an accretion disk luminosity or accretion power and this should only be considered as a general guideline. The bottom line is, however, that Sgr A* with its radio properties is not alone in the universe but is at the bottom end of the activity scale seen from supermassive black holes.

11.4 Imaging the Event Horizon - An Outlook

One can easily see from the previous sections that the ever growing interest in Sgr A* has already yielded a number of tantalizing results, the most important being that Sgr A* is the best supermassive black hole candidate

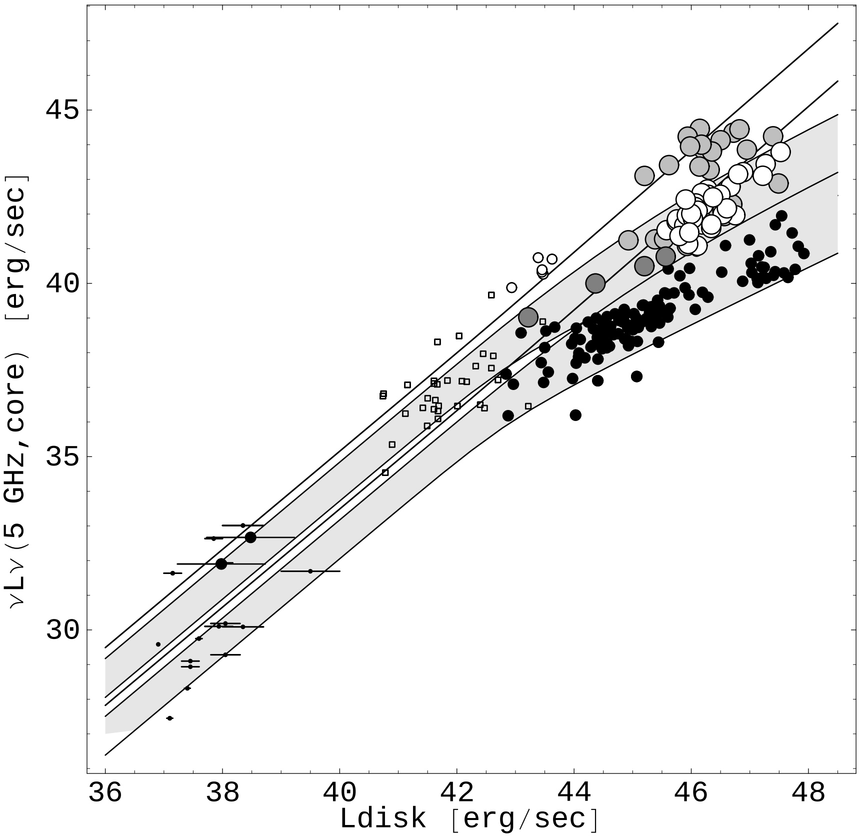

Figure 11.14 Correlation between thermal emission from the accretion disk (with the exception of X-ray binaries this is basically normalized to the narrow Hα emission) and the monochromatic luminosity of black hole radio cores. Open circles: Radio-loud quasars; small open circles: FR I radio galaxies; open gray circles: Blazars and radio-intermediate quasars (dark grey); black dots: radio-quiet quasars and Seyferts; small dots: X-ray binaries; small boxes: detected sources from the "48 LINERs" sample (Nagar et al. 2000). The latter apparently confirm the basic prediction of Falcke & Biermann (1996) and almost close the gap between very low (on an absolute scale) accretion rate objects and high accretion rate objects. The shaded bands represent the radio-loud and radio-quiet jet models as a function of accretion as shown in Falcke & Biermann (1996).

we know. VLBI observations are already approaching scales which are not far from the actual scale of the black hole and the presence of the submm-bump indicates that even more compact emission is present at yet smaller scales – possibly as close in as the event horizon of the black hole. It is therefore worth exploring whether we have in principle a chance to actually approach this scale with imaging techniques and to ask what we would expect to see. This naturally will have to be done at the highest radio frequencies where the resolution is the highest and the scatter-broadening of Sgr A* is the lowest.

At submm wavelengths, the various models indeed predict that the synchrotron emission of Sgr A* is not self-absorbed, allowing a view into the region near the event horizon. The size of this event horizon is $(1+\sqrt{1-a_*^2})R_g$, where $R_g \equiv GM/c^2$, M is the mass of the black hole, G is Newton's constant, c the speed of light, $a_* \equiv Jc/(GM^2)$ is the dimensionless spin of the black hole in the range 0 to 1, and J is the angular momentum of the black hole.

The appearance of the emitting region around a black hole was determined by Falcke, Melia, & Agol (2000) – from which we take the following discussion – under the condition that it is optically thin. For Sgr A* this might be the case for the submm-bump (Falcke et al. 1998) indicated by the turnover in the spectrum, and can always be achieved by going to a suitably high frequency. For the qualitative discussion the emissivity was assumed to be frequency independent and to be either spatially uniform or to scale as r^{-2}. These two cases cover a large range of conditions expected under several reasonable scenarios, be it a quasi-spherical infall, a rotating thick disk, or the base of an outflow. The calculations took into account all the well-known relativistic effects, e.g., frame dragging, gravitational redshift, light bending, and Doppler boosting.

For a planar emitting source behind a black hole, a closed curve on the sky plane divides a region where geodesics intersect the horizon from a region whose geodesics miss the horizon (Bardeen 1973)[5]. This curve, which is referred to as the "apparent boundary" of the black hole, is a circle of radius $\sqrt{27}R_g$ in the Schwarzschild case ($a_* = 0$), but has a more flattened shape of similar size for a Kerr black hole, slightly dependent on inclination. The size of the apparent boundary is much larger than the event horizon due to strong bending of light by the black hole. When the emission occurs in an optically thin region *surrounding* the black hole, the case of interest here, the apparent boundary has the same exact shape since the properties of the geodesics are independent of where the sources are located. However, photons on geodesics located within the apparent boundary that can still escape to the observer experience strong gravitational redshift and a shorter total path length, leading to a smaller integrated emissivity, while

[5] For the following discussion see also Chapter **??**

photons just outside the apparent boundary can orbit the black hole near the circular photon radius several times, adding to the observed intensity (Jaroszynski & Kurpiewski 1997). This produces a marked deficit of the observed intensity inside the apparent boundary – the "shadow" of the black hole.

We here consider a compact, optically-thin emitting region surrounding a black hole with spin parameter $a_* = 0$ (i.e., a Schwarzschild black hole) and a maximally spinning Kerr hole with $a_* = 0.998$. In the set of simulations shown in Fig. 11.15, the viewing angle i was taken to be $45°$ with respect to the spin axis (when it is present) with two distributions of the gas velocity v. The first has the plasma in free-fall, i.e., $v^r = -\sqrt{2r(a^2+r^2)}\Delta/A$ and $\Omega = 2ar/A$, where v^r is the Boyer-Lindquist radial velocity, Ω is the orbital frequency, $\Delta \equiv r^2 - 2r + a^2$, and $A \equiv (r^2+a^2)^2 - a^2\Delta\sin^2\theta$. (We have set $G = M = c = 1$ in this paragraph.) The second has the plasma orbiting in rigidly rotating shells with the equatorial Keplerian frequency $\Omega = 1/(r^{3/2}+a)$ for $r > r_{ms}$ with $v^r = 0$, and infalling with constant angular momentum inside $r < r_{ms}$ (Cunningham 1975), with $v^\theta = 0$ for all r.

In order to display concrete examples of how realistic the proposed measurements of these effects with VLBI will be, the expected images were simulated for the massive black hole candidate Sgr A* at the Galactic Center.

The results of the two different models with and without scattering at two different observing wavelengths are shown in Fig. 11.15. The two distinct features that are evident in the top panel for a rotating black hole are (1) the clear depression in I_ν – the shadow – produced near the black hole, which in this particular example represents a modulation of up to 90% in intensity from peak to trough, and (2) the size of the shadow, which here is $9.2R_{\rm g}$ in diameter. This represents a projected size of 34 μarcseconds. Such a resolution has already been surpassed in some λ2mm-VLBI experiments of other radio cores (Krichbaum et al. 2002). The shadow is a generic feature of various other models one can look at, including those with outflows, cylindrical emissivity, and various inclinations or spins.

This black hole shadow is also visible in the second illustrated case for a non-rotating black hole with a modulation in I_ν in the range of 50-75% from peak to trough, and with a diameter of roughly $10.4\,R_g$. In this case, the emission is asymmetric due to the strong Doppler shifts associated with the emission by a rapidly moving plasma along the line-of-sight (with velocity v_ϕ).

The important conclusion is that the diameter of the shadow – in marked contrast to the event horizon – is fairly independent of the black hole spin and is always of order $5R_{\rm s}$. The presence of a rotating hole viewed edge-on will lead to a shifting of the apparent boundary (by as much as 2.5 R_g, or 9 μarcseconds) with respect to the center of mass,

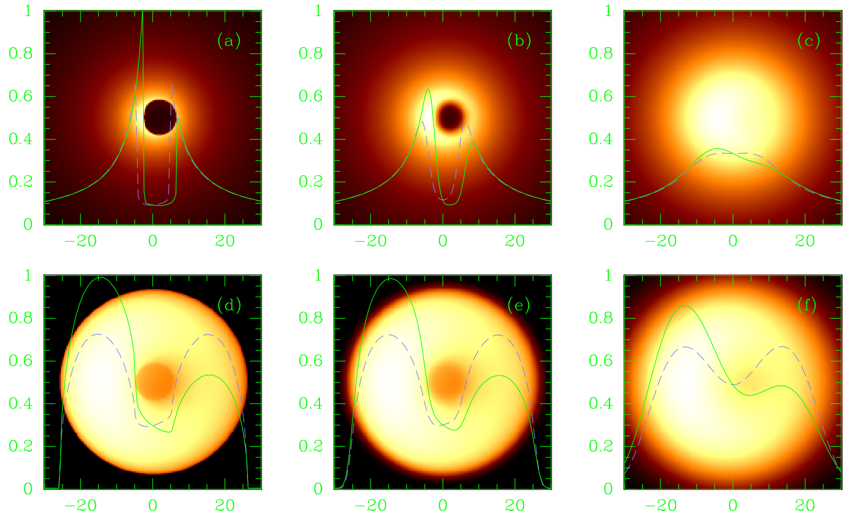

Figure 11.15 An image of an optically thin emission region surrounding a black hole with the characteristics of Sgr A* at the Galactic Center. The black hole is here either maximally rotating ($a_* = 0.998$, panels a-c) or non-rotating ($a_* = 0$, panels d-f). The emitting gas is assumed to be in free fall with an emissivity $\propto r^{-2}$ (top) or on Keplerian shells (bottom) with a uniform emissivity (viewing angle $i = 45°$). Panels a&d show the GR ray-tracing calculations, panels b&e are the images seen by an idealized VLBI array at 0.6 mm wavelength taking interstellar scattering into account, and panels c&f are those for a wavelength of 1.3 mm. The intensity variations along the x-axis (solid green curve) and the y-axis (dashed purple/blue curve) are overlayed. The vertical axes show the intensity of the curves in arbitrary units and the horizontal axes show the distance from the black hole in units of $GM_\bullet/c^2$ $(1/2R_\mathrm{s})$.

or the centroid of the outer emission region. Other possible signature of general relativistic effects may come from the polarization properties of the submm-wave emission region. This has been calculated by Bromley, Melia, & Liu (2001).

The importance of the proposed imaging of Sgr A* at submm wavelengths with VLBI cannot be overemphasized. The submm-bump in the spectrum of Sgr A* strongly suggests the presence of a compact component whose proximity to the event horizon is predicted to result in a shadow of measurable dimensions in the intensity map. Such a feature seems unique and Sgr A* seems to have all the right parameters to make it observable. The observation of this shadow would confirm the widely held belief that most of the dark mass concentration in the nuclei of galaxies such as ours is contained within a black hole, and it would be the first direct evidence for the existence of an event horizon largely independent of any modeling. *It would finally turn the theoretical concept of an event horizon discussed in the beginning of the book into an observable reality.*

A non-detection with sufficiently developed techniques, on the other hand, might pose a major problem for the standard black hole paradigm. Because of this fundamental importance, the experiment proposed here should be a major motivation for intensifying the current development of submm astronomy in general and mm- and submm-VLBI in particular.

This result also shows the outstanding position Sgr A* has among known radio cores and supermassive black hole candidates. For other supermassive black holes, with the exception perhaps of the very massive black hole in M87, the shadow will be much smaller than in Sgr A* because of the much larger distances.

REFERENCES

Agol, E. 2000, ApJ, 538, L121

Aitken, D. K., Greaves, J., Chrysostomou, A., Jenness, T., Holland, W., Hough, J. H., Pierce-Price, D., & Richer, J. 2000, ApJ, 534, L173

Backer, D. C., & Sramek, R. A. 1999, ApJ, 524, 805

Baganoff, F. K., Bautz, M. W., Brandt, W. N., Chartas, G., Feigelson, E. D., Garmire, G. P., Maeda, Y., Morris, M., Ricker, G. R., Townsley, L. K., & Walter, F. 2001, Nature, 413, 45

Balick, B., & Brown, R. L. 1974, ApJ, 194, 265

Bardeen, J. M. 1973, in Black Holes, ed. C. DeWitt & B. S. DeWitt (New York: Gordon & Breach), 215

Beckert, T., & Falcke, H. 2002, A&A, 388, 1106

Bietenholz, M. F., Bartel, N., & Rupen, M. P. 2000, ApJ, 532, 895

Bower, G. C., & Backer, D. C. 1998, ApJ, 496, L97

Bower, G. C., Backer, D. C., Zhao, J. H., Goss, M., & Falcke, H. 1999, ApJ, 521, 582

Bower, G. C., Falcke, H., & Backer, D. C. 1999, ApJ, 523, L29

Bower, G. C., Falcke, H., Sault, R. J., & Backer, D. C. 2002a, ApJ, 571, 843

Bower, G. C., Wright, M. C. H., Falcke, H., & Backer, D. C. 2002b, ApJ, submitted

Bridle, A. H., & Perley, R. A. 1984, ARA&A, 22, 319

Bromley, B. C., Melia, F., & Liu, S. 2001, ApJ, 555, L83

Brown, R. L., & Lo, K. Y. 1982, ApJ, 253, 108

Brunthaler, A., Bower, G. C., Falcke, H., & Mellon, R. R. 2001, ApJ, 560, L123

Cunningham, C. T. 1975, ApJ, 202, 788

Davies, R. D., Walsh, D., & Booth, R. S. 1976, MNRAS, 177, 319

Doeleman, S. S., Shen, Z. ., Rogers, A. E. E., Bower, G. C., Wright, M. C. H., Zhao, J. H., Backer, D. C., Crowley, J. W., Freund, R. W., Ho, P. T. P., Lo, K. Y., & Woody, D. P. 2001, AJ, 121, 2610

Falcke, H. 1996a, ApJ, 464, L67

Falcke, H. 1996b, in IAU Symp. 169: Unsolved Problems of the Milky Way, ed. L. Blitz & P. Teuben, Vol. 169 (Dordrecht: Kluwer), 169

Falcke, H. 1999, in ASP Conf. Ser. 186: The Central Parsecs of the Galaxy, ed. H. Falcke, A. Cotera, W. Duschl, F. Melia, & M. J. Rieke (San Francisco: Astronomical Society of the Pacific), 113

Falcke, H. 2001, Reviews of Modern Astronomy, 14, 15

Falcke, H., & Biermann, P. L. 1994, in Mass Transfer Induced Activity in Galaxies, ed. I. Shlosman (Cambridge University Press), 44

Falcke, H., & Biermann, P. L. 1995, A&A, 293, 665

Falcke, H., & Biermann, P. L. 1996, A&A, 308, 321

Falcke, H., & Biermann, P. L. 1999, A&A, 342, 49

Falcke, H., Goss, W. M., Matsuo, H., Teuben, P., Zhao, J. H., & Zylka, R. 1998, ApJ, 499, 731

Falcke, H., Malkan, M. A., & Biermann, P. L. 1995, A&A, 298, 375

Falcke, H., & Markoff, S. 2000, A&A, 362, 113

Falcke, H., Melia, F., & Agol, E. 2000, ApJ, 528, L13

Falcke, H., Nagar, N. M., Wilson, A. S., & Ulvestad, J. S. 2000, ApJ, 542, 197

Ferrari, A. 1998, ARA&A, 36, 539

Jaroszynski, M., & Kurpiewski, A. 1997, A&A, 326, 419

Königl, A. 1980, Physics of Fluids, 23, 1083

Krichbaum, T., et al. 2002, in Proceedings of the 6th European VLBI Network Symposium, ed. E. Ros, R. Porcas, A. Lobanov, & J. Zensus (Bonn, Germany: Max-Planck-Insitut für Radioastronomie), 125

Krichbaum, T. P., Graham, D. A., Witzel, A., Greve, A., Wink, J. E., Grewing, M., Colomer, F., de Vicente, P., Gomez-Gonzalez, J., Baudry, A., & Zensus, J. A. 1998, A&A, 335, L106

Krichbaum, T. P., Witzel, A., & Zensus, J. A. 1999, in ASP Conf. Ser. 186: The Central Parsecs of the Galaxy, ed. H. Falcke, A. Cotera, W. Duschl, F. Melia, & M. J. Rieke (San Francisco: Astronomical Society of the Pacific), 89

Krichbaum, T. P., et al. 1993, A&A, 274, L37

Lind, K. R., & Blandford, R. D. 1985, ApJ, 295, 358

Liu, S., & Melia, F. 2002, ApJ, 573, L23

Lo, K. Y., Shen, Z., Zhao, J. H., & Ho, P. T. P. 1999, in ASP Conf. Ser. 186: The Central Parsecs of the Galaxy, ed. H. Falcke, A. Cotera, W. Duschl, F. Melia, & M. J. Rieke (San Francisco: Astronomical Society of the Pacific), 72

Lo, K. Y., Shen, Z. Q., Zhao, J. H., & Ho, P. T. P. 1998, ApJ, 508, L61

Lynden-Bell, D., & Rees, M. J. 1971, MNRAS, 152, 461

Ma, C., Arias, E. F., Eubanks, T. M., Fey, A. L., Gontier, A.-M., Jacobs, C. S., Sovers, O. J., Archinal, B. A., & Charlot, P. 1998, AJ, 116, 516

Marcaide, J. M., Alberdi, A., Lara, L., Pérez-Torres, M. A., & Diamond, P. J. 1999, A&A, 343, 801

Markoff, S., Falcke, H., Yuan, F., & Biermann, P. L. 2001, A&A, 379, L13

Melia, F., & Falcke, H. 2001, ARA&A, 39, 309

Melia, F., Liu, S., & Coker, R. 2000, ApJ, 545, L117

Menten, K. M., Reid, M. J., Eckart, A., & Genzel, R. 1997, ApJ, 475, L111

Nagar, N. M., Falcke, H., Wilson, A. S., & Ho, L. C. 2000, ApJ, 542, 186

Narayan, R., Mahadevan, R., Grindlay, J. E., Popham, R. G., & Gammie, C. 1998, ApJ, 492, 554

Pacholczyk, A. G. 1970, Radio Astrophysics (San Francisco: W.H. Freeman and Company)

Palmer, P., & Goss, W. M. 1996, Galactic Center Newsletter, 2, 3

Pedlar, A., Anantharamaiah, K. R., Ekers, R. D., Goss, W. M., van Gorkom, J. H., Schwarz, U. J., & Zhao, J. 1989, ApJ, 342, 769

Quataert, E., & Gruzinov, A. 2000, ApJ, 545, 842

Reid, M. J., Readhead, A. C. S., Vermeulen, R. C., & Treuhaft, R. N. 1999, ApJ, 524, 816

Reuter, H. P., & Lesch, H. 1996, A&A, 310, L5

Rogers, A. E. E., Doeleman, S., Wright, M. C. H., Bower, G. C., Backer, D. C., Padin, S., Philips, J. A., Emerson, D. T., Greenhill, L., Moran, J. M., & Kellermann, K. I. 1994, ApJ, 434, L59

Rybicki, G. B., & Lightman, A. P. 1979, Radiative processes in astrophysics (New York, Wiley-Interscience, 1979. 393 p.)

Scheuer, P. 1968, Nature, 218, 920

Serabyn, E., Carlstrom, J., Lay, O., Lis, D. C., Hunter, T. R., & Lacy, J. H. 1997, ApJ, 490, L77

Tsuboi, M., Miyazaki, A., & Tsutsumi, T. 1999, in ASP Conf. Ser. 186: The Central Parsecs of the Galaxy, ed. H. Falcke, A. Cotera, W. Duschl, F. Melia, & M. J. Rieke (San Francisco: Astronomical Society of the Pacific), 105

van Langevelde, H. J., Frail, D. A., Cordes, J. M., & Diamond, P. J. 1992, ApJ, 396, 686

Wright, M. C. H., & Backer, D. C. 1993, ApJ, 417, 560

Wrobel, J. M., & Heeschen, D. S. 1984, ApJ, 287, 41

Yuan, F., Markoff, S., & Falcke, H. 2002, A&A, 383, 854

Yusef-Zadeh, F., Choate, D., & Cotton, W. 1999, ApJ, 518, L33

Yusef-Zadeh, F., Cotton, W., Wardle, M., Melia, F., & Roberts, D. A. 1994, ApJ, 434, L63

Zensus, J. A. 1997, ARA&A, 35, 607

Zhao, J., Bower, G. C., & Goss, W. M. 2001, ApJ, 547, L29

Zhao, J.-H., Young, K. H., McGary, R. S., Ho, P. T. P., Tsutsumi, T., Goss, W. M., & Bower, G. C. 2001, American Astronomical Society Meeting 199

Zylka, R., Mezger, P. G., Ward-Thompson, D., Duschl, W. J., & Lesch, H. 1995, A&A, 297, 83